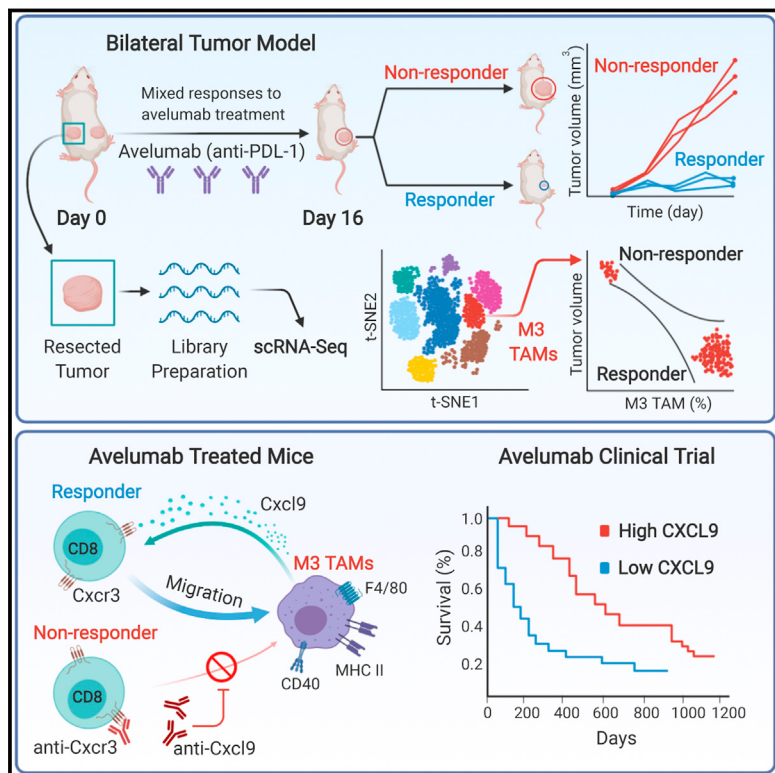


Cell Reports

Report

Baseline Frequency of Inflammatory Cxcl9-Expressing Tumor-Associated Macrophages Predicts Response to Avelumab Treatment

Graphical Abstract



Authors

Yan Qu, Ji Wen, Graham Thomas, ..., Xiao Wang, Shobha Potluri, Shahram Salek-Ardakani

Correspondence

shahram.salek-ardakani@pfizer.com

In Brief

Qu and colleagues combine a bilateral tumor model approach with scRNA-seq to identify immune cell types that predict response to the immune checkpoint inhibitor avelumab (anti-PD-L1). A Cxcl9-expressing, tumor-associated myeloid population is present in tumors before treatment and predicts a favorable outcome in pre-clinical and clinical studies.

Highlights

- CT26 cancer elicits a heterogeneous response to avelumab (anti-PD-L1) treatment
- A bilateral tumor model identifies cell types that predict response to avelumab
- A Cxcl9⁺ tumor-associated macrophage population predicts response to avelumab
- Blockade of Cxcl9 converts avelumab responders to non-responders



Report

Baseline Frequency of Inflammatory Cxcl9-Expressing Tumor-Associated Macrophages Predicts Response to Avelumab Treatment

Yan Qu,^{1,2} Ji Wen,^{1,2} Graham Thomas,^{1,2} Wenjing Yang,¹ Weiwei Prior,¹ Wenqian He,¹ Purnima Sundar,¹ Xiao Wang,¹ Shobha Potluri,^{1,3} and Shahram Salek-Ardakani^{1,3,4,*}

¹Cancer Immunology Discovery, Pfizer, Inc., 10777 Science Center Drive, San Diego, CA 92021, USA

²These authors contributed equally

³Senior author

⁴Lead Contact

*Correspondence: shahram.salek-ardakani@pfizer.com

<https://doi.org/10.1016/j.celrep.2020.107873>

SUMMARY

The tumor microenvironment is rich with immune-suppressive macrophages that are associated with cancer progression and resistance to immune checkpoint therapy. Using pre-treatment tumor biopsies complemented with single-cell RNA sequencing (RNA-seq), we characterize intratumoral immune heterogeneity to unveil potential mechanisms of resistance to avelumab (anti-PD-L1). We identify a proinflammatory F480⁺MHCII⁺Ly6C^{lo} macrophage population that is associated with response rather than resistance to avelumab. These macrophages are the primary source of the interferon-inducible chemokine Cxcl9, which facilitates the recruitment of protective Cxcr3⁺ T cells. Consequently, the efficacy of avelumab in mouse tumor models is dependent on Cxcr3 and Cxcl9, and baseline levels of Cxcl9 in patients treated with avelumab are associated with clinical response and overall survival. These data suggest that, within the broadly immune-suppressive macrophage compartment, a pro-inflammatory population exists that promotes responsiveness to PD-L1 blockade.

INTRODUCTION

Immune checkpoint blockade therapies (ICTs) targeting the programmed cell death 1 protein (PD-1)/programmed cell death 1 ligand 1 (PD-L1) axis have provided treatment opportunities for patients in a wide range of cancer indications by leveraging the immune system to control tumor growth. Avelumab is a clinical anti-PD-L1 antibody with murine cross-reactivity (Boyerinas et al., 2015; Hamilton and Rath, 2017). It is approved for the treatment of patients with metastatic Merkel cell carcinoma, advanced or metastatic urothelial carcinoma, and renal cell carcinoma (Kaufman et al., 2016; Motzer et al., 2019; Patel et al., 2018). While avelumab imparts durable responses in patients, only a subset of PD-L1-positive patients respond to treatment (Kaufman et al., 2016). Therefore, a better understanding of patient response profiles is required to identify clinically relevant predictive biomarkers and to develop rational combination therapies.

Successful ICT elicits CD8 T cell-dependent anti-tumor immunity; however, the suppressive tumor microenvironment can effectively mute these responses (Sharma and Allison, 2015). Tumor-associated macrophages (TAMs) are among the most abundant constituents of the tumor microenvironment (Qian and Pollard, 2010), and their presence is associated with a poor prognosis and resistance to ICT (Cassetta and Kitamura,

2018). Recent high-dimensional profiling analyses of tumor-infiltrating immune populations have unveiled considerable heterogeneity among TAMs (Chevrier et al., 2017; Zilionis et al., 2019). Currently, little is known about the roles of individual TAM subsets; however, there is evidence that some possess detrimental functions. For instance, a mass cytometry study of clear-cell renal cell carcinoma patients identified a CCL8⁺PD-L1⁺ TAM subset that associates with poor survival and T cell exhaustion (Chevrier et al., 2017).

Additionally, the frequency of a major histocompatibility complex class II^{low} (MHCII^{low}) myeloid phenotype in metastatic melanoma patients predicted a poor response to ICT (Krieg et al., 2018). As TAMs have generally been considered bad actors, clinical research programs aiming to deplete these cells or otherwise influence their function via recruitment or repolarization have attracted considerable interest (Cassetta and Kitamura, 2018). However, to date, clinical trials exploring TAM depletion have yielded little benefit (Peyraud et al., 2017), potentially because broad depletion strategies may affect both beneficial and immunosuppressive TAM subsets.

Using a bilateral tumor model that elicits a heterogeneous response to avelumab, we performed single-cell RNA sequencing (scRNA-seq) on tumor-associated immune cells before treatment to determine whether the pre-existing immune landscape influences responses to ICT. Surprisingly, we



discovered a TAM subset whose presence is predictive of successful ICT. This inflammatory TAM population expressed the T cell chemoattractant *Cxcl9*, high levels of the co-stimulatory receptor CD40 alongside MHCII, and the inflammatory biomarker *Cd38*. *Cxcl9* depletion prevented avelumab-mediated tumor rejection. Furthermore, in clinical cohorts receiving either the PD-L1 antagonist avelumab or atezolizumab, high *Cxcl9* expression is associated with an increase in median overall survival. These findings advance our understanding of TAM heterogeneity and function, showing that the TAM compartment contains host-protective subsets that serve as predictive biomarkers for successful ICT.

RESULTS

A Bilateral Tumor Model to Identify Biomarkers of Response to Anti-PD-L1 Treatment

To determine whether pre-existing tumor immune populations shape the response to avelumab, we identified syngeneic tumor models that elicit a partial response to treatment. Only CT26 colorectal carcinoma was determined to exhibit such heterogeneity, demonstrating a roughly 50% response rate (Figure S1A). In contrast, avelumab elicited responses in all mice bearing MC38 colorectal carcinoma (Figure S1B), while mice bearing either B16F10 melanoma or 4T1 breast cancer were both refractory to treatment (Figures S1C and S1D). We established a bilateral tumor model using CT26, reasoning that if immune profiles in contralateral tumors were similar, we could identify predictive correlates of response to treatment (Figure 1A). Equal numbers of CT26 cells were implanted into both flanks of BALB/c mice, and recipients with similarly sized tumors on each flank were enrolled onto observational study at 75 mm^3 ($\pm 20 \text{ mm}^3$), at which point, further analysis was undertaken. Initially, growth curve characterization was performed to determine the consistency in tumor growth and response to avelumab treatment between tumors on the same mouse. Left and right tumor volumes for both isotype-control- and avelumab-treated mice were significantly correlated (Figure 1B), confirming the predictive potential of the bilateral model. Furthermore, linearity was observed in tumor volumes between mice, regardless of treatment (Figure 1B), and, in an independent experiment, initial tumor volume was not found to influence growth rate (Figure S1E). Together, these findings imply that host-intrinsic factors significantly influence the underlying variability in CT26 growth rate and response to avelumab treatment.

Reasoning that differences in tumor immune microenvironments between mice influence growth, we performed scRNA-seq of CD45⁺ cells from 12 pairs of bilateral tumors 10 days post-implantation to assess the consistency in early tumor immune infiltration. 36 cell clusters were identified (including three CD45⁻ stromal cell clusters), many of which were significantly correlated between tumor flanks (Figure S1F). Hierarchical clustering analysis of these 36 cell cluster frequencies showed that individual mice indeed clustered together (Figure 1C) either as pairs or in small groups. Thus, host environmental factors significantly influence tumor immune responses at distant sites. Tumor volume had much less influence on the immune phenotype compared to host effects (Figures S1G and S1H). Of the 36 cell subsets, two statistically significant correlations exist vis-à-vis

tumor volume (Figure S1H). In contrast, 19 cell subset frequencies were significantly correlated at the same p value cutoff ($p < 0.05$) when comparing left and right flanks (Figure S1F). Thus, tumor immune profiles are consistent between flanks in bilaterally implanted mice, and tumor growth rates are significantly affected by host-intrinsic effects.

To explore whether the heterogeneous response of CT26 to avelumab was due to differences in baseline tumor immune composition, we coupled this bilateral tumor model with scRNA-seq to profile immune populations before treatment. Mice were implanted on both flanks, and tumors were grown to 78 mm^3 ($\pm 19 \text{ mm}^3$) before randomization (avelumab, n = 26; isotype, n = 10). Before treatment, one reference tumor on each mouse was surgically resected, and CD45⁺ cells were purified and processed for scRNA-seq. Mice were then treated with avelumab, and response was determined by the growth of the second tumor. We identified responders at day 16 as mice with tumors smaller than the smallest tumor observed in the isotype-control antibody-treated group, corresponding to a size of $\sim 500 \text{ mm}^3$ (Figure 1A).

scRNA-seq data from all 30 avelumab-treated mice were analyzed together to define the pretreatment immune landscape. Unbiased clustering of variable genes was performed, resulting in a total of 26 CD45⁺ clusters, which we visualized using uniform manifold approximation and projection (UMAP; Figure 1D). We did not observe the same number of clusters as in our preliminary scRNA-seq analysis of bilateral tumors sequenced on day 10. In both scRNA-seq studies, the tumors were sequenced at a consistent volume. Nevertheless, a higher number of CD8 T cell clusters were observed in our preliminary analysis of bilateral tumor pairs, which were sampled at day 10 post-implantation, compared to the single-flank avelumab response study, which was sampled at day 8. In the avelumab response study, there were two large meta-clusters relating to the lymphoid and myeloid lineages as well as a distinct cluster composed of plasmacytoid dendritic cells (DCs) (Figure 1D). The identity of these 26 clusters was curated by a manual review of known biomarkers (Figure 1E) and hierarchical clustering of differentially expressed genes (Figure 1F), which was found to segregate cell clusters into groups consistent with their annotated identities. We identified 10 clusters belonging to myeloid populations, which were found to cluster together. These included TAMs and monocytes that express the genes *Csf1r*, *Itgam* (CD11b), and *Adgre1* (F4/80) at differing intensities (M_1–M_10). Five clusters were assigned a DC phenotype: two clusters of conventional DCs identified as *Xcr1*⁺*Clec9a*⁺*Flt3*⁺ (DC_1) and *Xcr1*⁻*Clec9a*⁻*Flt3*⁺ (DC_3), which share characteristics of DC clusters DC1 and the newly described "mature DC enriched in immunoregulatory molecules" mregDC, defined by Maier et al. (2020); one myeloid DC cluster (DC_2), which, we determine, is analogous to subset DC2 in Maier et al. (2020); and two plasmacytoid DC clusters expressing *Siglech* and *Csf2rb* (DC_4 and DC_5). A further five clusters of T cells were identified. These include a mixed CD4/8-containing meta-cluster, T_1, that bears similarity to the group 1 tumor-infiltrating T cell signature defined by Magen et al. (2019), which was described to express *Cxcr6* and *Ifng*. CD4 T cell cluster T_3 expresses *Tbx21*, *Cxcr3*, and *Il7r*, possessing a expression profile similar to that of the group 2 tumor-infiltrating lymphocytes (TILs) defined by

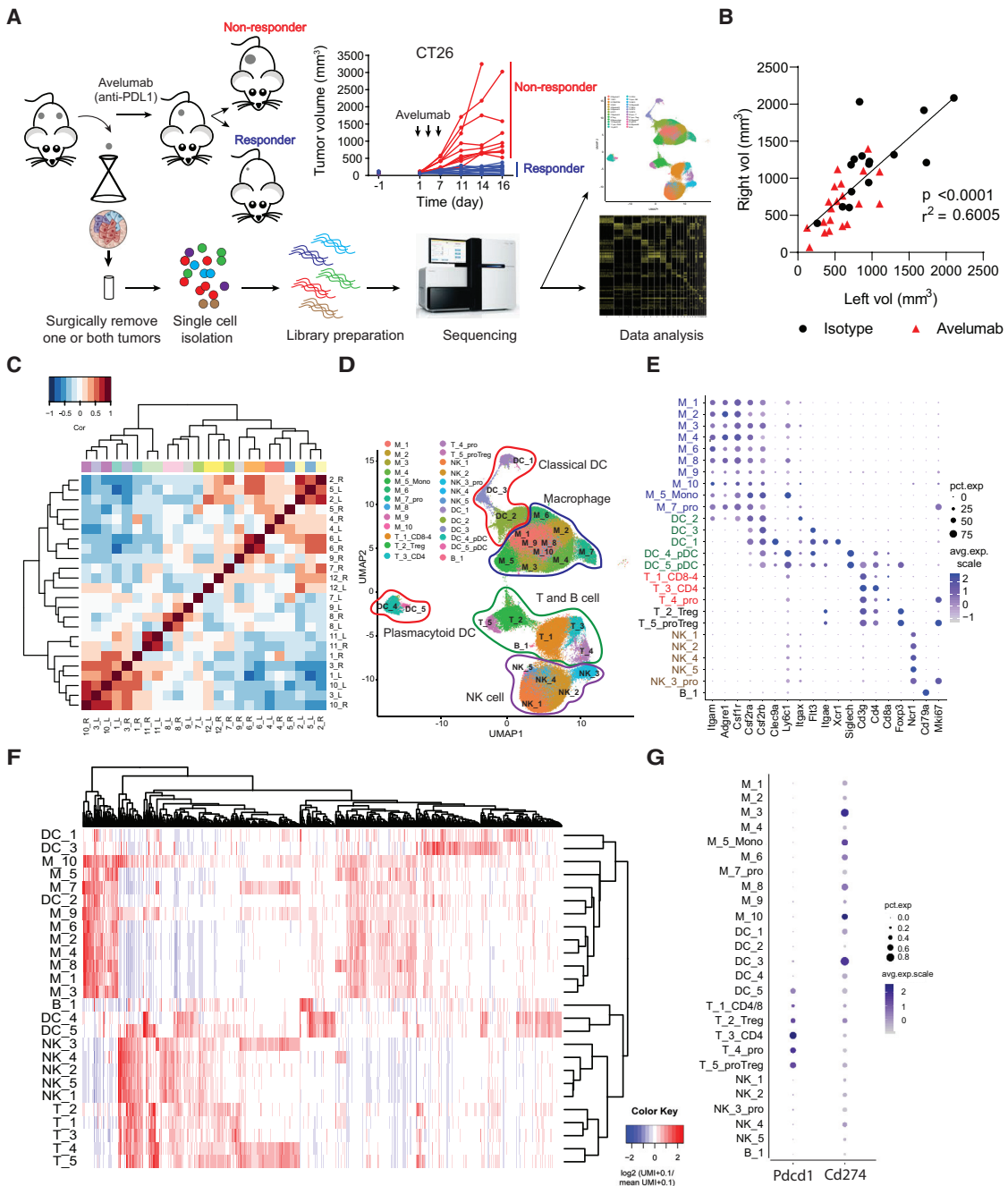


Figure 1. A Bilateral Tumor Model for Study of the Response to Anti-PD-L1 Treatment

(A) Schematic overview of the experimental design for the bilateral tumor response to avelumab.

(B) Correlation of bilateral CT26 tumor volumes 22 days post-implantation in isotype-control-treated (black) and avelumab-treated (10 mg/kg) mice. p value and correlation from linear regression are inset into figure.

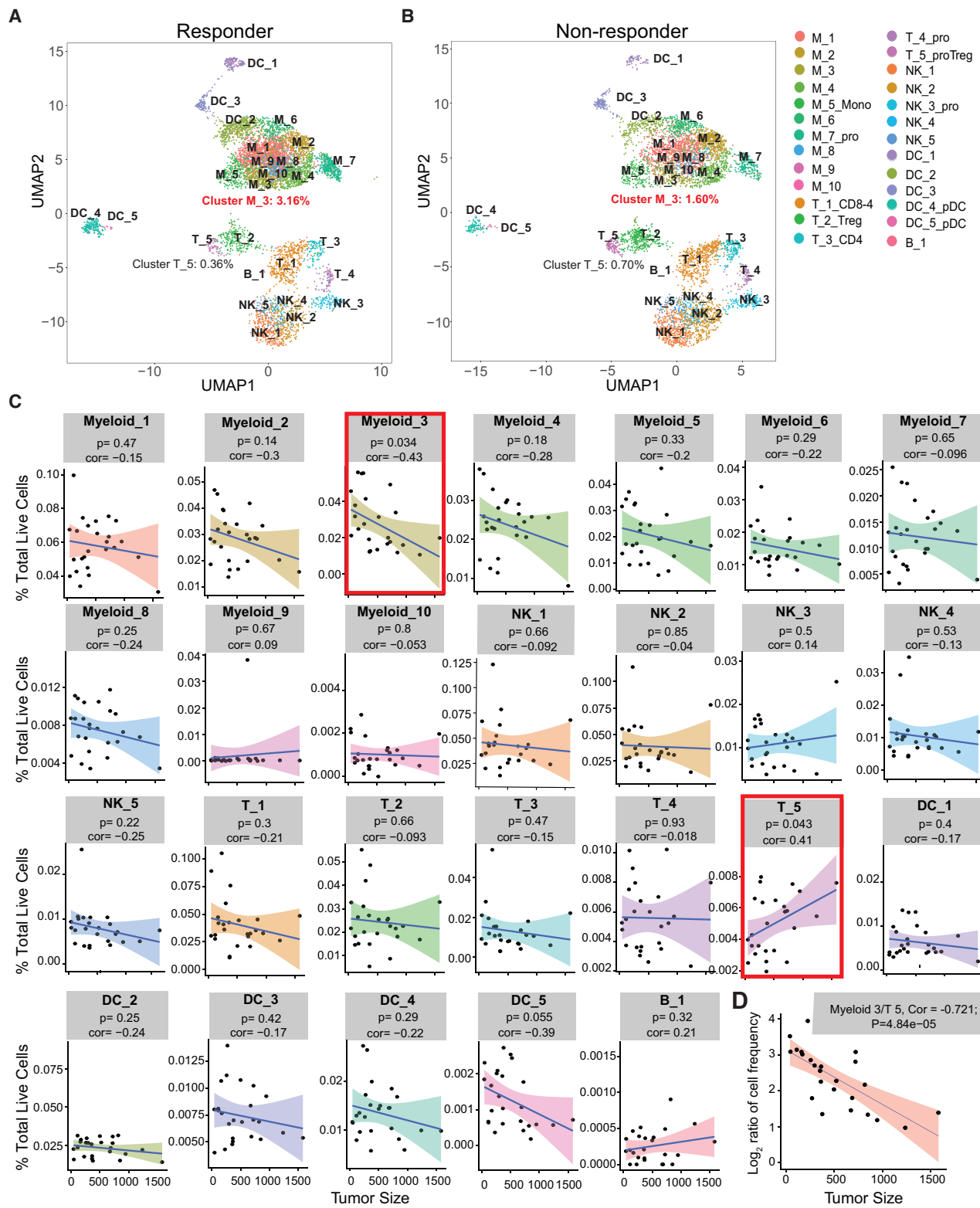
(C) Hierarchical clustering of immune cell population frequencies derived from scRNA-seq of 24 bilateral tumors excised from 12 mice. Colors in the color bar denote tumors derived from individual mice.

(D) UMAP visualization of 26 cell clusters identified from the scRNA-seq dataset.

(E) Manual annotation of scRNA-seq cell clusters using known marker genes to distinguish different cell types.

(F) Hierarchical clustering of genes assigned to scRNA-seq clusters that are enriched $>2.5 \times$ over background expression levels.

(G) Expression levels of the gene encoding PD-L1 (*Cd274*) and PD-1 (*Pdcd1*) in clusters. UMAP, uniform manifold approximation and projection.



(legend on next page)

Magen et al. (2019), while cluster T_4 contains a proliferation signature alongside a mix of both T_1 and T_3 genes. Finally, two clusters of *Foxp3*-positive, *Il2ra*-positive regulatory T cells (Treg, T_2 and T_5) were observed. Five clusters of natural killer (NK) cells (NK_1–NK_5) and one B cell cluster (B1) were also identified. In order to understand which populations in the tumor microenvironment (TME) may respond to avelumab, we examined the expression of PD-L1 (*Cd274*) and PD-1 (*Pdcd1*) in scRNA-seq clusters (Figure 1G). Low-level expression of PD-L1 was broadly observed, with a more abundant expression on macrophage population M_3 and on the *Xcr1*⁻*Clec9a*⁻*Flt3*^{+DC_3} cluster, whereas PD-1 expression was restricted to T cells (clusters T_2, -3, -4, and -5).

A TAM Subset Predicts Response to Avelumab Treatment

We tested whether cell populations exist before treatment that can discriminate between responders and non-responders to avelumab post-surgery. Using UMAP, several clusters were observed with altered density distributions, reflecting potential changes in the frequencies of these populations (Figures 2A and 2B). To capitalize on the variability in cell subset frequencies and responses, linear regression was performed by plotting the frequency of each cluster against the final tumor size after avelumab treatment. We did not observe any influence of starting tumor size in responder and non-responder populations (Figure S2A); however, as shown in Figure 2C, in 22 of 26 clusters, a weak negative correlation exists between cluster abundance and tumor size, implying that immune infiltration before treatment corresponds to a higher rate of response. Of the 26 clusters, only two were significantly associated with tumor size: myeloid cluster M_3 and Treg cluster T_5.

Myeloid cluster M_3 was positively associated with response to treatment ($R = -0.43$; $p = 0.03$) (Figure 2C); typically, mice with higher M_3 frequencies possessed smaller tumors. Stratifying mice into responder and non-responder populations reaffirmed this finding, showing that non-responders with the highest tumor volume following avelumab treatment possessed the fewest M_3 macrophages (Figure S2B). Treg cluster T_5, however, was negatively associated with outcome ($R = 0.41$; $p = 0.04$), consistent with the role of Tregs in impairing anti-tumor immunity.

Notably, T cell clusters T_4 and T_5, myeloid cluster M_7, and NK cluster N_3 possessed a proliferation profile defined by *mKi67* and *Top2a* expression (Figures S2C–S2E). Thus, a proliferating Treg signature before anti-PD-L1 treatment is associated with worse outcomes. To understand whether the frequency of proliferating Tregs could explain the presence of M_3, we investigated the correlation between these clusters and found that no such relationship exists ($R = 0.24$; $p = 0.2$; data not shown). However, the ratio of M_3 to T_5 was strongly predictive of tumor size ($R = -0.71$; $p < 0.001$; Figure 2D).

We questioned whether genes expressed by individual cell clusters were associated with response to avelumab treatment. We focused our analysis on cytokine and tumor necrosis factor (TNF) family members, reasoning that expression profiles of these critical immune regulators could provide insight into underlying molecular mechanisms associated with M_3 subset polarization. For each cluster, we identified gene expression profiles that significantly correlated with tumor volume and plotted a heatmap to visualize the correlations of significant gene expression profiles by cluster (Figure S2F). *Il10* was expressed by multiple TAM subsets (M_1, M_2, M_3, M_5, M_7, and M_8). It was found to be positively correlated with final tumor size (i.e., associated with non-response to treatment), as was the expression of the Th2 cytokine *Il5* by T cell clusters T_1 and T_3. However, *Ifng* production by proliferating T cell cluster T_4 or *Tnfsf9* (4-1BB-L) by multiple lymphocyte subsets (T_1, T_2, T_4, or NK_2) was found to be associated with a more favorable response to avelumab. Thus, the immune landscape of tumor immune microenvironment predisposes to anti-PD-L1 responsiveness. Furthermore, a pre-existing TAM population is associated with a favorable response to treatment. Differences in initial myeloid and Treg populations may coordinately regulate responses to immune checkpoint therapy.

Cxcl9⁺ TAMs Predict Responsiveness to Avelumab Therapy

The positive correlation between myeloid M_3 and response to avelumab prompted us to investigate the characteristics of this cluster that may underlie treatment response. First, we extracted the myeloid and DC clusters. We performed visualization using t-distributed stochastic neighbor embedding (t-SNE), which provided a more even distribution of the clusters to aid phenotyping (Figure 3A). We surveyed the expression of monocyte, M1-like, and M2-like macrophage lineage markers, including F4/80, CD11b, CD14, Ly6c, CD68, CD163, CD169, CD204, CD206, CD124, CCR2, CX3CR1, and CXCR4, and Fc γ receptors, including Fc γ RIIb, Fc γ RIII, and Fc γ IV. Most markers showed continuous expression spanning multiple myeloid populations (Figure 3B) that did not discriminate between the individual cell populations defined by clustering. To better understand the phenotypic heterogeneity of TAMs and monocytes, we performed unbiased hierarchical clustering of variable genes (Figure 3C) and single-cell trajectory analysis (Figure 3D). Each myeloid population possessed a distinct transcriptomic profile; however, similarities in TAM cluster gene expression observed by hierarchical clustering were also supported by trajectory analysis, showing that these different TAM subsets show differing degrees of similarity. Clusters M_7 and M_9 share a proliferation-associated signature, including expression of *Mki67*, *Top2a*, and *H2afx*, with M_7 expressing higher levels of these proliferation-associated genes (Figure 3C); clusters M_2 and M_4 possess a regulatory macrophage gene expression profile that includes *Folr2*, *Maf*, *Retnla*,

Figure 2. A TAM Subset Predicts Response to Avelumab Treatment

(A and B) UMAP visualization showing the density distribution of cells within clusters between responders (A) and non-responders (B).

(C) Correlation analysis plotting the frequency of cells in each cluster against final tumor size after avelumab treatment. The M_3 and T_5 clusters significantly associated with response are highlighted in red boxes. Linear regression p values and correlation values are inset into the figure.

(D) Linear regression analysis of M_3/T_5 cluster frequency ratio against final tumor volume. p value and correlation value are inset into the figure.

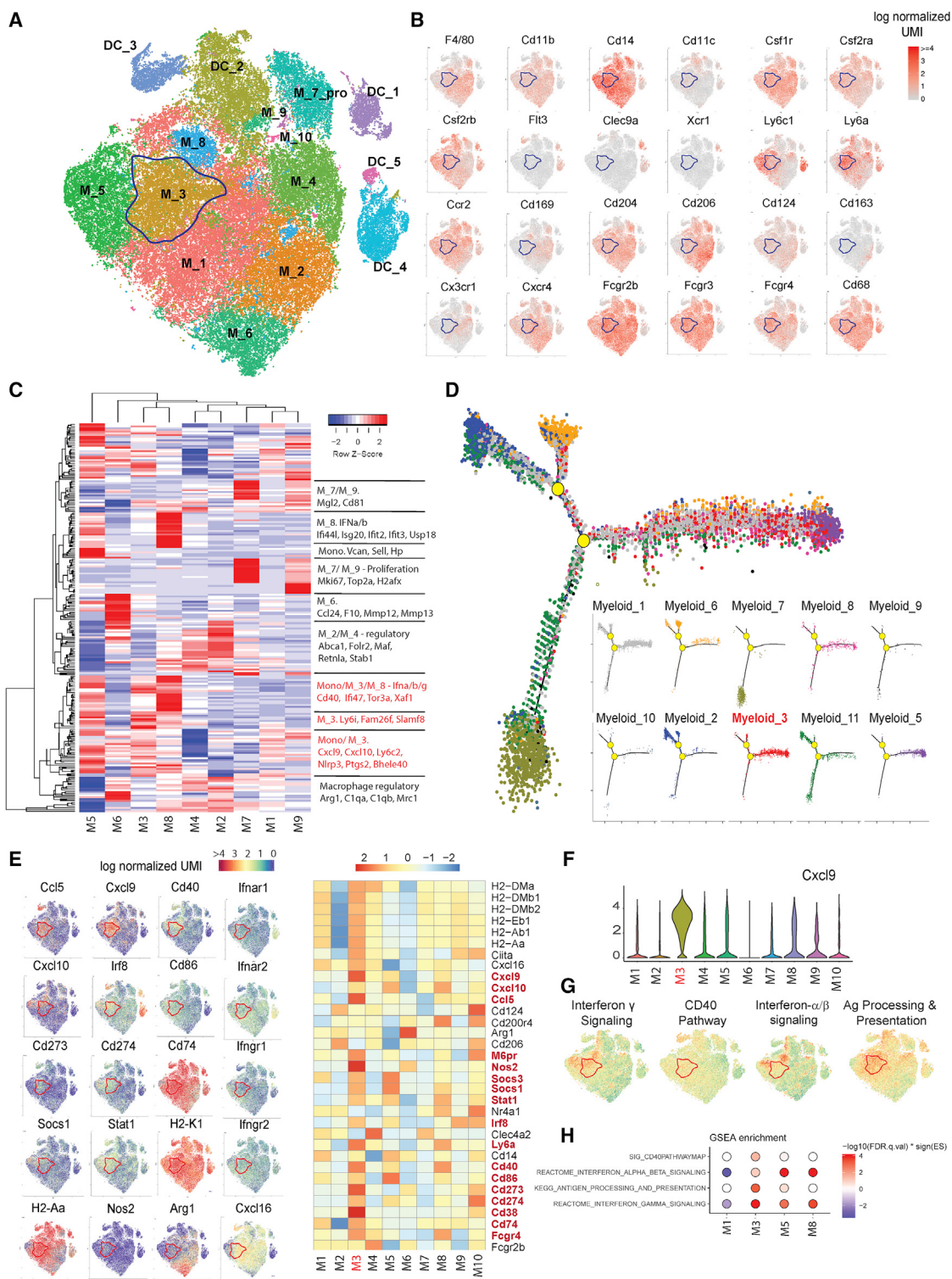


Figure 3. Cxcl9⁺ Monocyte-Derived TAMs Predict Responsiveness to Anti-PD-L1 Therapy

- (A) t-SNE plot of all myeloid subset cells. Cluster M_3 is highlighted with a blue contour line.
- (B) t-SNE plots showing the relative expression of monocyte and macrophage lineage markers in TAM and DC clusters.
- (C) Hierarchical clustering of genes that are differentially expressed between TAM clusters.
- (D) Single-cell trajectory analysis revealing the relationships among myeloid clusters. TAMs are plotted as merged together (upper) or separately (lower inset).

(legend continued on next page)

Arg1, and *Mrc1* as well as complement factors *C1qa* and *C1qb*; cluster M_6, however, also includes the *Arg1* and *Mrc1* gene expression cluster in addition to tissue remodeling genes, including *Mmp12* and *Mmp13*. Cluster M_5 was identified to be composed of monocytes, uniquely expressing *Vcan* and *Sell*. M_5 shared a large cluster of genes with M_3 and M_8 TAMs, implying that these subsets may be recently monocyte derived. These genes include *Ly6C2*, *Nlrp3*, *Cxcl9*, and *Cxcl10* (Figure 3C). The single-cell trajectory analysis also positions the M_3 and M_8 populations on the same branch as M_5 monocytes, further implying that these cells may have recent monocytic origins (Figure 3D). Interestingly, clusters M_3 and M_8 share an overlapping interferon (IFN)-associated gene signature, which includes *Cd40* and *Ifi47*. However, M_8 expresses additional type-1 IFN-associated genes, including *Ifi44l*, *Isg20*, *Ifit2*, *Ifit3*, and *Usp18*, that are not observed in the M_3 population.

To better understand how M_3 may control responses to avelumab, we identified genes associated with M_3 compared with other TAMs. We discovered an activation profile, with *Cxcl9* being the most definitive gene for M_3 (Figures 3E, 3F, and S3A). A broader inflammatory signature, including *Cd40*, *Ccl5*, *M6pr*, *Cd38*, *Ly6a*, *Cd74*, and *MHCII* gene expression, was also more abundant in M_3 than in other myeloid populations (Figures 3E). Gene set enrichment analysis identified myeloid-activation-associated pathways in M_3, showing enriched IFN- γ with relatively less IFN- α/β pathway utilization (Figures 3G, 3H, and S3B). This was supported by visualization of representative type-1 and type-2 IFN-associated genes *Cxcl9* and *Cxcl10*, respectively, showing relatively higher expression of *Cxcl9* in M_3 macrophages yet higher *Cxcl10* expression in M_8 TAMs (Figures 3F and S3C). Nuclear factor κ B (NF- κ B) and antigen-presentation-associated gene were also upregulated in M_3 TAMs, however, also observed in additional TAM subsets (Figures 3G, S3B, and S3D). Together, these data strongly imply that IFN- γ regulates M_3 polarization.

As M_3 macrophages correlate with response to avelumab treatment, we assessed the frequencies of M_3 macrophages in other syngeneic models. We pooled and clustered scRNA-seq data for MC38, 4T1, and CT26 and identified M_3 macrophages as the *Cxcl9*- and *Cd40*-expressing cluster 9 (Figures S4A and S4B). Consistent with the avelumab-responsive nature of MC38 and CT26, higher frequencies of M_3 macrophages were observed relative to the refractory 4T1 tumors; furthermore, the range of M_3 frequencies covering both responsive and non-responsive tumors in CT26 spans the range between 4T1 and MC38 (Figure S4C). Strikingly, in gene lists recently published examining human TAM signatures by scRNA-seq, one subset of TAMs, “M9,” shares notable similarity with TAM cluster M_3, containing *Cxcl9*, *Cxcl10*, *Ccl5*, *MHCII*, *Cd40*, and *Stat1* (Zilionis et al., 2019), seeming to provide a human ortholog to M_3. We queried the similarity of these subsets by performing enrichment analysis, comparing the overlap of gene lists defined for murine myeloid clusters M_1–M_10 to human TAM and

monocyte subset gene lists defined by Zilionis et al. (2019) (Figure S4D). Many TAM subsets do not directly align in a one-to-one relationship, perhaps owing to species- and tissue-specific differences in macrophage polarization phenotypes as previously noted by Zilionis et al (2019). As expected, however, we observe substantial overlap between classical monocyte gene sets in both our mouse and the Zilionis human datasets, consistent with the conserved one-to-one relationship between species (Zilionis et al. 2019). Importantly, a similar highly significant intersection of gene lists is observed between the M_3 gene list we define here and the M9 signature defined by Zilionis et al. (2019) (Figure S4D), indicating that the M_3 TAM subset is conserved between species. In summary, we define an inflammatory TAM population expressing *Cxcl9* that appears to be present in both human and mouse that, in our preclinical model, is predictive of the response to avelumab treatment.

Cxcl9 Expression Determines Sensitivity to Anti-PD-L1 Treatment

To define components of the M_3 inflammatory gene signature that may contribute to the anti-tumor functions of these cells, we interrogated clinical trial datasets for the PD-L1 antagonists avelumab and atezolizumab. We stratified patients into cohorts based upon expression of the M_3-associated genes *Cxcl9*, *Cxcl10*, and *Cd40* and assessed survival by Kaplan-Meier analysis. Strikingly, for avelumab (Figure 4A) and atezolizumab (Figure 4B), respectively, we observed a 2.4- and 2.8-fold increase in median overall survival in patients with the highest *Cxcl9* expression compared with those in the lowest expressing quantile. We also observed a significant, albeit less profound, increase in survival times in patients with higher *Cxcl10* expression in the atezolizumab trial (Figures 4C and 4D); however, this trend was not observed for *Cd40* expression levels (Figures 4E–4H). *Cxcl9* and *Cxcl10* are ligands for *Cxcr3*. *Cxcr3* is required by T cells for effective antitumor immunity (Chow et al., 2019; Mikucki et al., 2015). Given these clinical observations and our understanding that M_3 macrophages are the primary source of *Cxcl9* before treatment with anti-PD-L1 (Figure S3A), we tested the role of *Cxcl9* in mediating the response to avelumab. Mice were implanted on a single flank with CT26 tumors and pretreated with an anti-CXCL9 blocking antibody before avelumab treatment and monitored for tumor growth. Anti-CXCL9 treatment alone had no impact on tumor growth (Figure 4I). However, the CXCL9 blockade abolished tumor growth inhibition caused by avelumab (Figure 4I). Consistently, inhibition of CXCL9 signaling by antagonizing the counterpart receptor CXCR3 yielded similar results (Figure 4J). Collectively, these findings demonstrate that a pre-existing inflammatory macrophage signature predetermines responsiveness to anti-PD-L1 checkpoint therapy, that the *Cxcl9* axis is a key determinant of responsiveness to avelumab, and that *Cxcl9* expression may be a key facet of M_3 TAM biology.

(E) t-SNE plots of marker genes upregulated in M_3 macrophages (highlighted in red contour) and heatmap gene expression of select immunologically relevant genes upregulated in M_3 TAMs.

(F) Violin plot showing the expression of *Cxcl9* in TAM subsets

(G and H) t-SNE plots (G) and GSEA enrichment scores (H) showing the projected pathway enrichment significantly enriched pathways in cluster M_3.

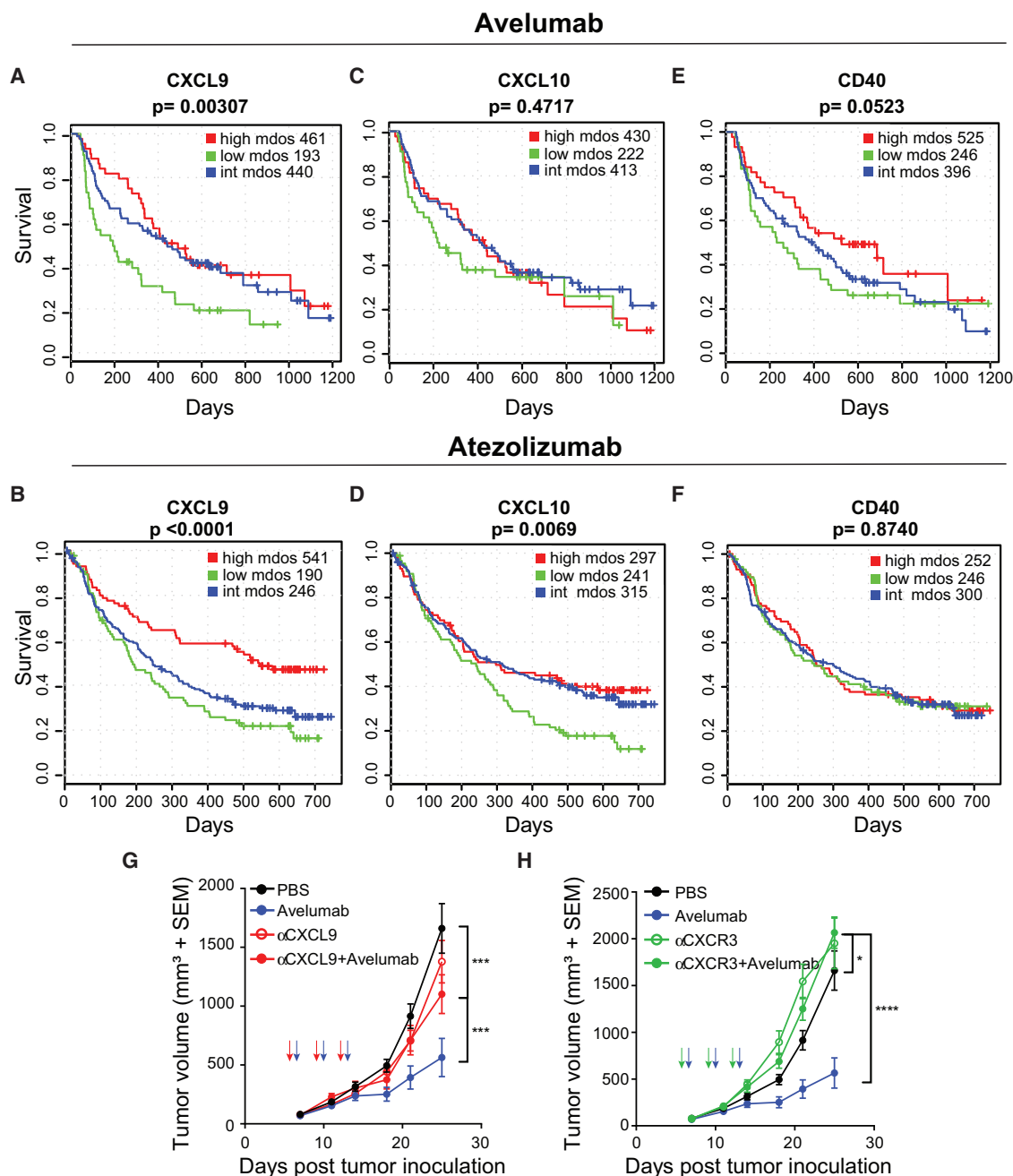


Figure 4. Cxcl9 Expression Is Required For Anti-PD-L1 Efficacy

(A–H) Clinical data from two anti-PD-L1 trials, IMvigor210, a phase II trial of atezolizumab (A, C, and E) in platinum-treated locally advanced or metastatic ur-othelial carcinoma, and EMR 100070-001, a phase I study of avelumab (B, D, and F) in multiple solid tumor indications. (A and B) Cxcl9, (C and D) Cxcl10, (E and F) Cd40. Reported p values are from a Cox proportional hazard ratio test comparing the highest (red lines) and lowest (green lines) quartiles of gene expression; intermediate gene expression values are indicated (blue lines). MDOS, median days overall survival. (G and H) Tumor-bearing animals were dosed with either anti-CXCL9 (G, red arrows) or anti-CXCR3 (H, green arrows) antibodies prior to avelumab treatment ($n = 10$ per group). Anti-Cxcl9 and anti-Cxcr3 antibodies were dosed at 10 mg/kg 1 day prior to avelumab (dosed at 20 mg/kg), as indicated by arrows (red, anti-Cxcl9; green, anti-Cxcr3; blue, avelumab). Data were analyzed using 2-way ANOVA with Tukey's correction for multiple testing. * $p < 0.05$; ** $p < 0.001$; *** $p < 0.0001$.

DISCUSSION

The transformation to malignancy of cancerous cells requires evasion of the homeostatic mechanism of immune surveillance

(Kim et al., 2007). Tumors establish a suppressive microenvironment comprising TAMs and Tregs to escape these surveillance mechanisms. In this study, we addressed whether aspects of this inhibitory milieu were associated with resistance to ICT.

Surprisingly, rather than inhibitory markers, we identified an inflammatory *Cxcl9*⁺*MHCII*⁺*Cd40*⁺ TAM population that correlates with responses to avelumab. Predictive biomarkers of ICT success include tumor mutational burden, PD-L1 expression, and CD8 T cell infiltration (Hugo et al., 2016; Roh et al., 2017; Snyder et al., 2014; Van Allen et al., 2015); these either contribute to, or are regulated by IFN- γ signaling. Our pathway enrichment analysis suggests that IFN- γ regulates M_3 *Cxcl9* expression; however, IFN- γ gene signatures were also observed in the M_8 TAM and M_5 monocyte populations, yet neither of these predicts avelumab response. Thus, additional factors may coincide with IFN- γ signaling to maintain M_3 TAMs and sensitize to ICT. Such additional processes would be predicted to facilitate the expression of genes that discriminate M_3 TAMs from the M_5 and M_8 populations, including MHCII and *Cxcl9*. Thus, M_3 TAMs may represent a more precise predictive biomarker of ICT success than simply upstream IFN- γ -associated pathways.

Data from two clinical trials show that patients with high *Cxcl9* expression have improved survival during anti-PD-L1 blockade. We also identified an M_3-like macrophage in human TAMs that express *Cxcl9* and many other key M_3-associated marker genes (Zilionis et al., 2019). This M_3 ortholog was correlated with a poor prognosis in the lung adenocarcinoma data presented by Zilionis et al. (2019). However, in the underlying dataset used in this publication, *Cxcl9* expression associated with a favorable prognosis across all cancers (Gentles et al., 2015), highlighting the relevance of M_3 TAMs to anti-tumor responses in specific indications. Dangaj et al. (2019) recently showed that myeloid-derived *Cxcl9* supports favorable outcomes in multiple indications. *Cxcl9* expressed by peri-tumoral macrophages correlated with intra-tumoral CD8 T cell infiltration.

Further supporting these clinical observations, pre-clinical studies highlight the role of *Cxcl9*-expressing myeloid cells and DCs in mediating ICT-dependent anti-tumor T cell responses. Chow et al. (2019) showed that anti-PD-1 enhances DC *Cxcl9* expression, which contributes to the efficacy of anti-PD-1 therapy. Additionally, using a positron-emission tomography-based approach, Rashidian et al. (2019) segregated anti-PD-1-treated mice into predicted responder and non-responder groups, using an early T cell infiltration signature. scRNA-seq profiling of these anti-PD-1-treated cohorts showed that an early IFN- γ signature in the TAM compartment is associated with a favorable outcome. Our work extends these findings by showing that a pre-existing *Cxcl9*-expressing M_3 myeloid population correlates with anti-PD-L1 efficacy and that the presence of such a population may be required for the initial infiltration of IFN- γ -expressing cells following ICT that later give rise to broad *Cxcl9* expression across the TAM and DC compartment observed following treatment (Chow et al., 2019; Rashidian et al., 2019). Thus, initial *Cxcl9* expression levels may be a critical rate-limiting step for effective anti-tumor immunity. While literature suggests that CD8 T cell-derived IFN- γ facilitates the myeloid M_3 activation phenotype, key outstanding questions are whether M_3 macrophages are causally associated with response to immune checkpoint blockade therapy; if so, which additional cellular or molecular processes may govern this initial M_3 polarization; and whether proliferating regulatory CD4+ T cells impair such processes.

Our analysis of single-cell trajectory data suggests that inflammatory *Cxcl9*-expressing TAMs are monocyte derived, consistent with the notion that these protective TAMs represent a component of peripheral immune surveillance. Other groups have published scRNA-seq and mass cytometry studies of tumor myeloid populations and also have reported ongoing infiltration and differentiation of monocyte-derived macrophages within the TAM compartment (Li et al., 2019; Loyher et al., 2018). This suggests that, at least for some subsets of TAMs, a continuous monocyte recruitment and differentiation process is a common feature of tumor macrophage biology. Notably, our analysis of TIL cytokine expression profiles showed that *Il10* production by TAMs is associated with non-response to avelumab. Recent studies have highlighted the fact that reducing suppressive TAM polarization, either by inhibiting tumor-derived suppressive factors such as *Lif* or by depletion approaches, leads to increased monocytic infiltration and TAM *Cxcl9* expression, which contribute to the control of tumor growth (Etzerodt et al., 2019; Pascual-García et al., 2019).

Further work is needed to understand the factors and pathways that give rise to the M_3 gene expression modules for *Cxcl9* and MHCII and whether the loss of M_3 TAMs was a direct result of tumor-induced immune suppression. The identification of anti-tumor TAM subsets required for effective immunotherapy challenges the notion that all TAM subsets are bad actors. Importantly, it may explain the limited efficacy of macrophage colony-stimulating factor inhibitors that broadly deplete macrophages. Novel treatment approaches directed at modulating tumor TAM immune suppression will need to consider these nuances.

STAR★METHODS

Detailed methods are provided in the online version of this paper and include the following:

- **KEY RESOURCES TABLE**
- **RESOURCE AVAILABILITY**
 - Lead Contact
 - Materials Availability
 - Data and Code Availability
- **EXPERIMENTAL MODEL AND SUBJECT DETAILS**
 - Animals
 - Cell lines
- **METHOD DETAILS**
 - Subcutaneous Tumor Models in Mice
 - Tumor CD45+ cell purification, single-Cell RNA-Seq library preparation and sequencing
 - Prognostic Impact of CXCL9 for Anti-PD-L1 Therapy in Clinical Samples
- **QUANTIFICATION AND STATISTICAL ANALYSIS**
 - Tumor volume quantification
 - scRNA-Seq Gene Expression Quantification
 - Single-Cell Clustering and Annotation
 - Cell Cluster Frequency Calculation
 - Calculation of Correlation to Tumor Size
 - scRNA-Seq assessment of immune subset infiltration in bilateral tumor pairs

- Myeloid Cell Heterogeneity Analysis
- Identification of human cell correlate to M_3

SUPPLEMENTAL INFORMATION

Supplemental Information can be found online at <https://doi.org/10.1016/j.celrep.2020.107873>.

ACKNOWLEDGMENTS

The authors thank Lora Zhao, Dilduz Telman, Sophanna Kong, Min Liao, Breanna Jung, Teresa Radcliffe, German Vergara, Andrew Jimena, Chris Van-devert, Peter Schow, Caroline Gundel, and Tuan Ngo for technical assistance and Keith Ching for assistance with survival analysis. Proofreading of the manuscript was performed by Carissa Vardanian at ClinicalThinking and funded by Pfizer and Merck.

AUTHOR CONTRIBUTIONS

Y.Q., S.P., G.T., P.S., and S.S.-A. designed the experiments; Y.Q., W.P., W.H., and P.S. performed the experiments; Y.Q., J.W., G.T., W.P., W.Y., W.H., X.W., S.P., and S.S.-A. analyzed data; and G.T., Y.Q., J.W., and S.S.-A. wrote the manuscript.

DECLARATION OF INTERESTS

All authors are Pfizer employees and may hold stock/stock options in the company. This study was funded by Pfizer as part of an alliance between Pfizer and Merck, Darmstadt, Germany. Pfizer employees plan to file a patent application relating to this work.

Received: September 27, 2019

Revised: March 30, 2020

Accepted: June 15, 2020

Published: July 7, 2020; corrected online August 21, 2020

REFERENCES

- Becht, E., McInnes, L., Healy, J., Dutertre, C.A., Kwok, I.W.H., Ng, L.G., Ginhoux, F., and Newell, E.W. (2018). Dimensionality reduction for visualizing single-cell data using UMAP. *Nat. Biotechnol.* Published December 3, 2018. <https://doi.org/10.1038/nbt.4314>.
- Boyerinas, B., Jochems, C., Fantini, M., Heery, C.R., Gulley, J.L., Tsang, K.Y., and Schlom, J. (2015). Antibody-Dependent Cellular Cytotoxicity Activity of a Novel Anti-PD-L1 Antibody Avelumab (MSB0010718C) on Human Tumor Cells. *Cancer Immunol. Res.* 3, 1148–1157.
- Butler, A., Hoffman, P., Smibert, P., Papalexi, E., and Satija, R. (2018). Integrating single-cell transcriptomic data across different conditions, technologies, and species. *Nat. Biotechnol.* 36, 411–420.
- Cassetta, L., and Kitamura, T. (2018). Targeting Tumor-Associated Macrophages as a Potential Strategy to Enhance the Response to Immune Checkpoint Inhibitors. *Front. Cell Dev. Biol.* 6, 38.
- Chevrier, S., Levine, J.H., Zanotelli, V.R.T., Silina, K., Schulz, D., Bacac, M., Ries, C.H., Ailles, L., Jewett, M.A.S., Moch, H., et al. (2017). An Immune Atlas of Clear Cell Renal Cell Carcinoma. *Cell* 169, 736–749.e18.
- Chow, M.T., Ozga, A.J., Servis, R.L., Frederick, D.T., Lo, J.A., Fisher, D.E., Freeman, G.J., Boland, G.M., and Luster, A.D. (2019). Intratumoral Activity of the CXCR3 Chemokine System Is Required for the Efficacy of Anti-PD-1 Therapy. *Immunity* 50, 1498–1512.e5.
- Dangaj, D., Bruand, M., Grimm, A.J., Ronet, C., Barras, D., Duttagupta, P.A., Lanitis, E., Duraiswamy, J., Tanyi, J.L., Benencia, F., et al. (2019). Cooperation between Constitutive and Inducible Chemokines Enables T Cell Engraftment and Immune Attack in Solid Tumors. *Cancer Cell* 35, 885–900.e810.
- Etzerodt, A., Tsalkitzis, K., Maniecki, M., Damsky, W., Delfini, M., Baudoin, E., Moulin, M., Bosenberg, M., Graversen, J.H., Auphan-Anezin, N., et al. (2019). Specific targeting of CD163⁺ TAMs mobilizes inflammatory monocytes and promotes T cell-mediated tumor regression. *J. Exp. Med.* 216, 2394–2411.
- Gentles, A.J., Newman, A.M., Liu, C.L., Bratman, S.V., Feng, W., Kim, D., Nair, V.S., Xu, Y., Khuong, A., Hoang, C.D., et al. (2015). The prognostic landscape of genes and infiltrating immune cells across human cancers. *Nat. Med.* 21, 938–945.
- Hamilton, G., and Rath, B. (2017). Avelumab: combining immune checkpoint inhibition and antibody-dependent cytotoxicity. *Expert Opin. Biol. Ther.* 17, 515–523.
- Hugo, W., Zaretsky, J.M., Sun, L., Song, C., Moreno, B.H., Hu-Lieskovay, S., Berent-Maoz, B., Pang, J., Chmielowski, B., Cherry, G., et al. (2016). Genomic and Transcriptomic Features of Response to Anti-PD-1 Therapy in Metastatic Melanoma. *Cell* 165, 35–44.
- Kaufman, H.L., Russell, J., Hamid, O., Bhatia, S., Terheyden, P., D'Angelo, S.P., Shih, K.C., Lebbé, C., Linette, G.P., Milella, M., et al. (2016). Avelumab in patients with chemotherapy-refractory metastatic Merkel cell carcinoma: a multicentre, single-group, open-label, phase 2 trial. *Lancet Oncol.* 17, 1374–1385.
- Kim, R., Emi, M., and Tanabe, K. (2007). Cancer immunoediting from immune surveillance to immune escape. *Immunology* 121, 1–14.
- Krieg, C., Nowicka, M., Guglietta, S., Schindler, S., Hartmann, F.J., Weber, L.M., Dummer, R., Robinson, M.D., Levesque, M.P., and Becher, B. (2018). High-dimensional single-cell analysis predicts response to anti-PD-1 immunotherapy. *Nat. Med.* 24, 144–153.
- Kurtulus, S., Madi, A., Escobar, G., Klapholz, M., Nyman, J., Christian, E., Pawlak, M., Dionne, D., Xia, J., Rozenblatt-Rosen, O., et al. (2019). Checkpoint Blockade Immunotherapy Induces Dynamic Changes in PD-1(-)CD8(+) Tumor-Infiltrating T Cells. *Immunity* 50, 181–194.e6.
- Li, H., van der Leun, A.M., Yofe, I., Lubling, Y., Gelbard-Solodkin, D., van Akkooi, A.C.J., van den Braber, M., Rozeman, E.A., Haanen, J., Blank, C.U., et al. (2019). Dysfunctional CD8 T Cells Form a Proliferative, Dynamically Regulated Compartment within Human Melanoma. *Cell* 176, 775–789.e18.
- Loyer, P.L., Hamon, P., Laviron, M., Meghraoui-Kheddar, A., Goncalves, E., Deng, Z., Torstensson, S., Bercovici, N., Baudesson de Chanville, C., Combadière, B., et al. (2018). Macrophages of distinct origins contribute to tumor development in the lung. *J. Exp. Med.* 215, 2536–2553.
- Magen, A., Nie, J., Ciucci, T., Tamoutounour, S., Zhao, Y., Mehta, M., Tran, B., McGavern, D.B., Hannenhalli, S., and Bosselut, R. (2019). Single-Cell Profiling Defines Transcriptomic Signatures Specific to Tumor-Reactive versus Virus-Responsive CD4(+) T Cells. *Cell Rep.* 29, 3019–3032.e6.
- Maier, B., Leader, A.M., Chen, S.T., Tung, N., Chang, C., LeBerichel, J., Chudnovskiy, A., Maskey, S., Walker, L., Finnigan, J.P., et al. (2020). A conserved dendritic-cell regulatory program limits antitumour immunity. *Nature* 580, 257–262.
- Mikucki, M.E., Fisher, D.T., Matsuzaki, J., Skitzki, J.J., Gaulin, N.B., Muhitch, J.B., Ku, A.W., Frelinger, J.G., Odunsi, K., Gajewski, T.F., et al. (2015). Non-redundant requirement for CXCR3 signalling during tumoricidal T-cell trafficking across tumour vascular checkpoints. *Nat. Commun.* 6, 7458.
- Motzer, R.J., Penkov, K., Haanen, J., Rini, B., Albiges, L., Campbell, M.T., Venugopal, B., Kollmannsberger, C., Negrier, S., Uemura, M., et al. (2019). Avelumab plus Axitinib versus Sunitinib for Advanced Renal-Cell Carcinoma. *N. Engl. J. Med.* 380, 1103–1115.
- Pascual-García, M., Bonfill-Tejedor, E., Planas-Rigol, E., Rubio-Perez, C., Iurillo, R., Arias, A., Cuartas, I., Sala-Hojman, A., Escudero, L., Martínez-Ricarte, F., et al. (2019). LIF regulates CXCL9 in tumor-associated macrophages and prevents CD8⁺ T cell tumor-infiltration impairing anti-PD1 therapy. *Nat. Commun.* 10, 2416.
- Patel, M.R., Ellerton, J., Infante, J.R., Agrawal, M., Gordon, M., Aljumaily, R., Britten, C.D., Dirix, L., Lee, K.W., Taylor, M., et al. (2018). Avelumab in metastatic urothelial carcinoma after platinum failure (JAVELIN Solid Tumor): pooled results from two expansion cohorts of an open-label, phase 1 trial. *Lancet Oncol.* 19, 51–64.

- Peyraud, F., Cousin, S., and Italiano, A. (2017). CSF-1R Inhibitor Development: Current Clinical Status. *Curr. Oncol. Rep.* **19**, 70.
- Qian, B.Z., and Pollard, J.W. (2010). Macrophage diversity enhances tumor progression and metastasis. *Cell* **141**, 39–51.
- Rashidian, M., LaFleur, M.W., Verschoor, V.L., Dongre, A., Zhang, Y., Nguyen, T.H., Kolifrath, S., Aref, A.R., Lau, C.J., Paweletz, C.P., et al. (2019). Immuno-PET identifies the myeloid compartment as a key contributor to the outcome of the antitumor response under PD-1 blockade. *Proc. Natl. Acad. Sci. USA* **116**, 16971–16980.
- Roh, W., Chen, P.L., Reuben, A., Spencer, C.N., Prieto, P.A., Miller, J.P., Gopalakrishnan, V., Wang, F., Cooper, Z.A., Reddy, S.M., et al. (2017). Integrated molecular analysis of tumor biopsies on sequential CTLA-4 and PD-1 blockade reveals markers of response and resistance. *Sci. Transl. Med.* **9**, eaah3560.
- Sharma, P., and Allison, J.P. (2015). The future of immune checkpoint therapy. *Science* **348**, 56–61.
- Snyder, A., Makarov, V., Merghoub, T., Yuan, J., Zaretsky, J.M., Desrichard, A., Walsh, L.A., Postow, M.A., Wong, P., Ho, T.S., et al. (2014). Genetic basis for clinical response to CTLA-4 blockade in melanoma. *N. Engl. J. Med.* **371**, 2189–2199.
- Trapnell, C., Cacchiarelli, D., Grimsby, J., Pokharel, P., Li, S., Morse, M., Lennon, N.J., Livak, K.J., Mikkelsen, T.S., and Rinn, J.L. (2014). The dynamics and regulators of cell fate decisions are revealed by pseudotemporal ordering of single cells. *Nat. Biotechnol.* **32**, 381–386.
- Van Allen, E.M., Miao, D., Schilling, B., Shukla, S.A., Blank, C., Zimmer, L., Sucker, A., Hillen, U., Foppen, M.H.G., Goldinger, S.M., et al. (2015). Genomic correlates of response to CTLA-4 blockade in metastatic melanoma. *Science* **350**, 207–211.
- Zilionis, R., Engblom, C., Pfirschke, C., Savova, V., Zemmour, D., Saatcioglu, H.D., Krishnan, I., Maroni, G., Meyerovitz, C.V., Kerwin, C.M., et al. (2019). Single-Cell Transcriptomics of Human and Mouse Lung Cancers Reveals Conserved Myeloid Populations across Individuals and Species. *Immunity* **50**, 1317–1334.e10.

STAR★METHODS

KEY RESOURCES TABLE

REAGENT or RESOURCE	SOURCE	IDENTIFIER
Antibodies		
Avelumab	Merck Serono (Darmstadt, Germany)	Lot No. 508203
Human immunoglobulin G1 isotype control antibody	Pfizer, Inc	Lot No. NB123249p192CA110124
Hamster IgG anti-Cxcr3	Bioxcell	Cxcr3-173; RRID:AB_2687730
Hamster IgG anti-Cxcl9	Bioxcell	MIG-2F5.5; RRID:AB_2736989
Rat IgG2b anti-mouse CD45	Biolegend (CA, USA)	30-F11; RRID:AB_312976
Fixable viability dye eFluor 506	Thermo Fisher (CA, USA)	65-0866-14
Critical Commercial Assays		
Mouse tumor dissociation kit	Myltenyi Biotech (Germany)	130-096-730
Chromium Single Cell 5' Library and Gel Bead Kit	10x Genomics (CA, USA)	1000092
Deposited Data		
Study data are deposited in GEO	NCBI GEO (https://www.ncbi.nlm.nih.gov/geo/)	GEO: GSE150970
Zilionis et al.	NCBI GEO (https://www.ncbi.nlm.nih.gov/geo/)	GEO: GSE127465
Experimental Models: Cell Lines		
CT26 colorectal carcinoma	ATCC	CRL-2638
Experimental Models: Organisms/Strains		
BALB/c female mice 6-8 weeks old	Jackson laboratories (ME)	000651
Software and Algorithms		
Cell Ranger	10x Genomics (CA, USA)	v2.1.1
Seurat	Butler et al. 2018	v2.3.3 & v3.1.0
Monocle	Trapnell et al. 2014	v2.6.4

RESOURCE AVAILABILITY

Lead Contact

Further information and requests for resources and reagents should be directed to and will be fulfilled by the Lead Contact, Shahram Salek-Ardakani (Shahram.Salek-Ardakani@pfizer.com)

Materials Availability

This study did not generate unique reagents

Data and Code Availability

Original data have been deposited to NCBI GEO: GSE150970.

EXPERIMENTAL MODEL AND SUBJECT DETAILS

Animals

Six- to 8-week-old female BALB/c mice were purchased from Jackson Laboratories (Bar Harbor, ME). All animals were housed in a pathogen-free vivarium facility at Pfizer Inc (South San Francisco and San Diego, CA), and experiments were conducted according to protocols in accordance with the Institutional Animal Care and Use Committee (IACUC) guidelines.

Cell lines

The CT26 colon carcinoma cell line was purchased from American Type Culture Collection (ATCC CRL-2638; Manassas, VA). Cells were cultured in Dulbecco's Modified Eagle Medium supplemented with 10% fetal bovine serum and 100 IU/mL

penicillin-streptomycin at 37°C in an atmosphere of 5% carbon dioxide and IMPACT tested for pathogens at the Research Animal Diagnostic Laboratory (Columbia, MO). Pathogen-free cells in exponential growth phase were harvested and used for tumor inoculation.

METHOD DETAILS

Subcutaneous Tumor Models in Mice

BALB/c mice were inoculated subcutaneously on both flanks with an equal number of CT26 cells ($1\text{--}5 \times 10^5$) in 0.1 mL of phosphate-buffered saline (PBS). For the scRNA-Seq avelumab response study mice were randomized when and one tumor resected when tumors volume reached $78 \pm 19.1 \text{ mm}^3$. Thirty animals were recruited to the avelumab treatment group and 10 to the isotype control antibody group. Treatment was started 24 hours after surgery. For the bilateral response to avelumab treatment study mice were treated day 10 post-injection (the same time point for the initial study), here tumors were $75\text{mm}^3 \pm 20 \text{ mm}^3$. Body weight was recorded weekly. Avelumab was provided by Merck Serono (Darmstadt, Germany; Lot No. 508203). Human immunoglobulin G1 isotype control antibody was prepared in-house (Lot No. NB123249p192CA110124). Antibodies were prepared at a concentration of 1 mg/mL in PBS and dosed at 0.1 mL per mouse intraperitoneally for a total of three doses every 3 days. For CXCL9 and CXCR3 blocking studies antibodies were administered at 10 mg/kg with injections performed one day prior to avelumab administration. For blocking antibody studies, we used anti-Cxcr3 clone Cxcr3-173 (Bioxcell) and anti-Cxcl9 clone MIG-2F5.5 (Bioxcell).

Tumor CD45+ cell purification, single-Cell RNA-Seq library preparation and sequencing

Harvested tumors were dissociated to obtain single-cell suspensions using the mouse tumor dissociation kit (Miltenyi Biotec; Bergisch Gladbach, Germany) according to the manufacturer's protocol, except for Enzyme R, which was used at a 1:10 dilution of the protocol recommendation. For the scRNA-Seq avelumab response experiment, dissociated tumor cells were measured using Vi-CELL (Beckman Coulter; Brea, CA), and $1\text{--}5 \times 10^6$ cells were stained using fluorescently labeled mouse CD45 antibody (clone 30F11) and Fixable Viability Dye eFluor 506 (Thermo Fisher Scientific; Waltham, MA) to sort for live CD45⁺ and CD45⁻ cells using the FACSAria II cell sorter (BD Biosciences; San Jose, CA). Approximately $5.5\text{--}111 \times 10^3$ viable CD45⁺ cells were sorted with an 85-μm nozzle using default settings directly into round-bottomed polystyrene collection tubes containing 500 μL PBS with 0.5% bovine serum albumin (BSA). Sorted CD45⁺ cells were counted using the Cellometer K2 Viability Cell Counter (Nexcelom; Lawrence, MA) prior to loading on a Chromium Single Cell Chip (10x Genomics; Pleasanton, CA). For the bilateral paired scRNA-Seq study dissociated cells were filtered through 70 μm and 40 μm cell strainers and incubated with MACS Miltenyi CD45 TIL microbeads (Cat# 130-110-618). Thereafter, CD45⁺ cells were isolated using the MACS Miltenyi multiMACS Cell Separator Plus (Cat# 130-098-637), all according to manufacturer instructions. All cell counts were performed using the Beckman Coulter ViCell XR (Cat# 731050). Following counts, cells were resuspended in 0.04% BSA in PBS at a concentration of 1e6 cells/ml. Approximately 16×10^3 viable cells were loaded onto a Chromium Single Cell A Chip (10x Genomics) to aim for target cell recovery of 10^4 cells. Library construction was performed using 50 ng cDNA following the Chromium Single Cell 5' Library and Gel Bead Kit protocol (10x Genomics). Libraries were sequenced using the NovoSeq 6000 platform (Illumina; San Diego, CA).

Prognostic Impact of CXCL9 for Anti-PD-L1 Therapy in Clinical Samples

To assess the association of CXCL9 expression with overall survival, we performed univariate survival analysis on CXCL9 expression in baseline tumors from two anti-PD-L1 clinical trials: IMvigor210, a phase II trial of atezolizumb in platinum-treated locally advanced or metastatic urothelial carcinoma, and EMR 100070-001, an EMD Serono phase I study of avelumab in solid tumors. From Cox proportional hazards regression, high expression of CXCL9 was associated with better overall survival in both studies. For IMvigor210, there were baseline tumor samples from 348 patients, and clinical information and CXCL9 expression were obtained from the R package IMvigor210CoreBiology. For EMR 100070-001, there were baseline tumor samples from 173 patients. In each dataset, we divided the samples into three groups: CXCL9 high (greater than upper quantile), CXCL9 intermediate (less than upper quantile and greater than lower quantile), and CXCL9 (less than lower quantile).

QUANTIFICATION AND STATISTICAL ANALYSIS

Tumor volume quantification

Tumor size was measured in two dimensions using a digital caliper, and the volume was expressed in cubic millimeters using the formula $V = 0.5 \times (L \times W^2)$ where L and W are the long and short diameters of the tumor, respectively.. Percentage of tumor growth inhibition was defined as $[1 - (\text{Tumor volume}_{\text{Treated}} / \text{Tumor volume}_{\text{Isotype control}})] \times 100$. Percentage of weight loss was defined as $[1 - (\text{Body weight}_{\text{Treated}} / \text{Body weight}_{\text{Isotype control}})] \times 100$. For tumor growth inhibition studies tumor volumes differences between groups were compared by 2-way ANOVA using PRISM software (Graphpad).

scRNA-Seq Gene Expression Quantification

scRNA-Seq data were processed using the Cell Ranger v2.1.1 (10x Genomics) to generate count-level data for further analysis. Each lane of cells was processed independently using the Cell Ranger count. The unique molecular identifier (UMI) counts for each sample

were then merged using Seurat v2.3.3, requiring that the number of expressed genes for each cell was > 200 and < 5000 . Cells with $> 10\%$ of UMI originated from mitochondrial genes were removed. Genes expressed in at least three cells were kept and then normalized and scaled using the default setting in Seurat.

Single-Cell Clustering and Annotation

For each sample, we selected the top 2000 highly variable genes (HVG). These genes were combined into 3756 HVG for downstream analysis. Canonical correlation analysis (CCA) ([Butler et al., 2018](#)) was then performed to align cells belonging to the same cell type across different samples using the top 20 CCA components. Cell clustering was performed on the aligned CCA space. To find out the optimal cluster numbers, we repeated the clustering process using a sequence of resolution parameter from 0.2 to 1 in increments of 0.2, with larger values leading to a greater number of clusters. The optimal clustering was determined by the lowest increase in the cluster number when comparing each of two adjacent resolutions, which indicated a relatively stable result (Figure S1). This procedure generated 28 cell clusters at resolution 1.0. The cell identity was determined by manual review of top differentially expressed genes in each cell cluster. Two small CD45⁻ cell clusters indicating tumor or stromal cell contamination were removed from further analysis.

Cell Cluster Frequency Calculation

For each sample, we calculated the frequency of cell cluster i in sample j as $f_{ij} = n_{ij} / \sum_{i=1}^{26} n_{ij}$, where n_{ij} is the number of cells of cluster i in sample j calculated from our single cell sequencing dataset, and $\sum_{i=1}^{26} n_{ij}$ is the total number of CD45⁺ cells sequenced in sample j . For simplicity, we named this frequency as %in45. Of note, it might be misleading when directly using this number in downstream analysis. First, because $\sum_{i=1}^{26} f_{ij} = 1$, it is not surprising to find a cluster's frequency going down, while another cell type's frequency going up. Second, different mice had different tumor sizes when measured even prior to treatment; however, single-cell sequencing protocols require a similar number of CD45⁺ cells collected for different samples. The value of %in45 without considering tumor size cannot faithfully reflect the profile of immune infiltration in tumors. To solve this issue, we instead calculated the percentage value of a cell cluster relative to the total live cell count prior to enrichment, named %inT, or % total live cells, in our downstream analysis. Specifically, %inT was defined as m_{ij}/M_j , where m_{ij} is the number of cells of cluster i in tumor sample j , and M_j is the total number of all type of cells in tumor sample collected. M_j can be expressed as sum of CD45⁺ cells M_j^{CD45+} and CD45⁻ cells M_j^{CD45-} . Thus, %inT can be calculated as $((m_{ij}/M_j) = (m_{ij}/M_j^{CD45+})(M_j^{CD45+}/M_j))$. In scRNA-Seq, a subset of M_j^{CD45+} has been collected and sequenced, thus f_{ij} is an unbiased estimator of m_{ij}/M_j^{CD45+} . The second term in the equation was derived from FACS when doing the cell sorting.

Calculation of Correlation to Tumor Size

For each single-cell cluster, the correlation between %inT value of each cell cluster and tumor size were tested using linear regression. For all possible pairs of cell clusters, we calculated the log₂ ratio of the two %inT values, then linear regression was applied to test the association between the log₂ ratio and tumor size.

scRNA-Seq assessment of immune subset infiltration in bilateral tumor pairs

Bilateral implantations, scRNA-Seq cell and library preparation and sequence data processing were performed as outlined above. Cell subset (cluster) frequencies defined based on automated cluster annotation calls were enumerated for within each tumor sample and linear regression analysis was performed to evaluate tumor infiltrating immune cell subsets between tumor pairs on the same mouse, or against tumor volume for each individual tumor. For hierarchical clustering analysis cell subset frequencies were standardized by subtracting the population mean from each cluster and dividing mean-centered values by row standard deviation to account for differences in cluster frequency abundance. A pairwise correlation matrix was calculated to compare infiltration profiles between individual tumors and heatmap visualization performed using complete linkage clustering hierarchical clustering or euclidian distance estimates.

Myeloid Cell Heterogeneity Analysis

Cell clusters originating from myeloid lineage populations were extracted from the CD45⁺ cells for further analysis. t-SNE was applied to the myeloid lineage cells using Seurat. Due to the higher reproducibility and better meaningful organization of cell clusters ([Becht et al., 2018](#)), we chose the UMAP technique in our initial visualization of CD45⁺ cell clusters. The unsupervised single-cell trajectory for myeloid cell clusters was constructed in Monocle v2.6.4 ([Trapnell et al., 2014](#)), using the top 1000 differentially expressed genes. Gene Set Enrichment Analysis (GSEA) was applied to find pathway difference between C5 and other myeloid cell clusters. For better visualization in t-SNE, we defined a pathway score for each single cell using a similar method to [Kurtulus et al. \(2019\)](#). First, the data were scaled (z-score across each gene) to remove bias toward highly expressed genes. Then, for each cell, a score was computed by first sorting the scaled expression value for each cell followed by summing up the indices of the pathway genes. For hierarchical clustering analysis differentially expressed genes were identified between all pairwise clusters, we selected genes that were differentially expressed between each TAM cluster and any other TAM cluster and further filtered genes whose expression was less than 2-fold greater than median TAM expression levels and an absolute expression level lower than 1 UMI. Row (gene) standardized expression levels were subject to hierarchical clustering for visualization.

Identification of human cell correlate to M_3

To examine correlates of M_3 macrophages in human datasets, gene expression data were downloaded from GSE127465 ([Zillionis et al., 2019](#)). Differentially expressed genes in each cluster form Zillionis et al. were calculated using Seurat v3.1.0 with the following parameters min.pct = 0.5, logfc.threshold = 0.25,p_va_adj = 0.05. Macrophage populations defined in the human dataset were compared with mouse macrophage subsets by mapping human and mouse gene identifiers using biomaRt. Similarities scores between gene lists for myeloid clusters in each dataset were compared by Fishers' exact test.

Update

Cell Reports

Volume 32, Issue 9, 1 September 2020, Page

DOI: <https://doi.org/10.1016/j.celrep.2020.108115>

Correction

Baseline Frequency of Inflammatory Cxcl9-Expressing Tumor-Associated Macrophages Predicts Response to Avelumab Treatment

Yan Qu, Ji Wen, Graham Thomas, Wenjing Yang, Weiwei Prior, Wenqian He, Purnima Sundar, Xiao Wang, Shobha Potluri, and Shahram Salek-Ardakani*

*Correspondence: shahram.salek-ardakani@pfizer.com

<https://doi.org/10.1016/j.celrep.2020.108115>

(Cell Reports 32, 107873-1–107873-11.e1–e4; July 7, 2020)

In the originally published version of this paper, Figure 3A contained some incorrectly labeled dendritic cell populations. The figure has been updated, and the corrected figure now appears here and with the paper online.

The authors regret this error.



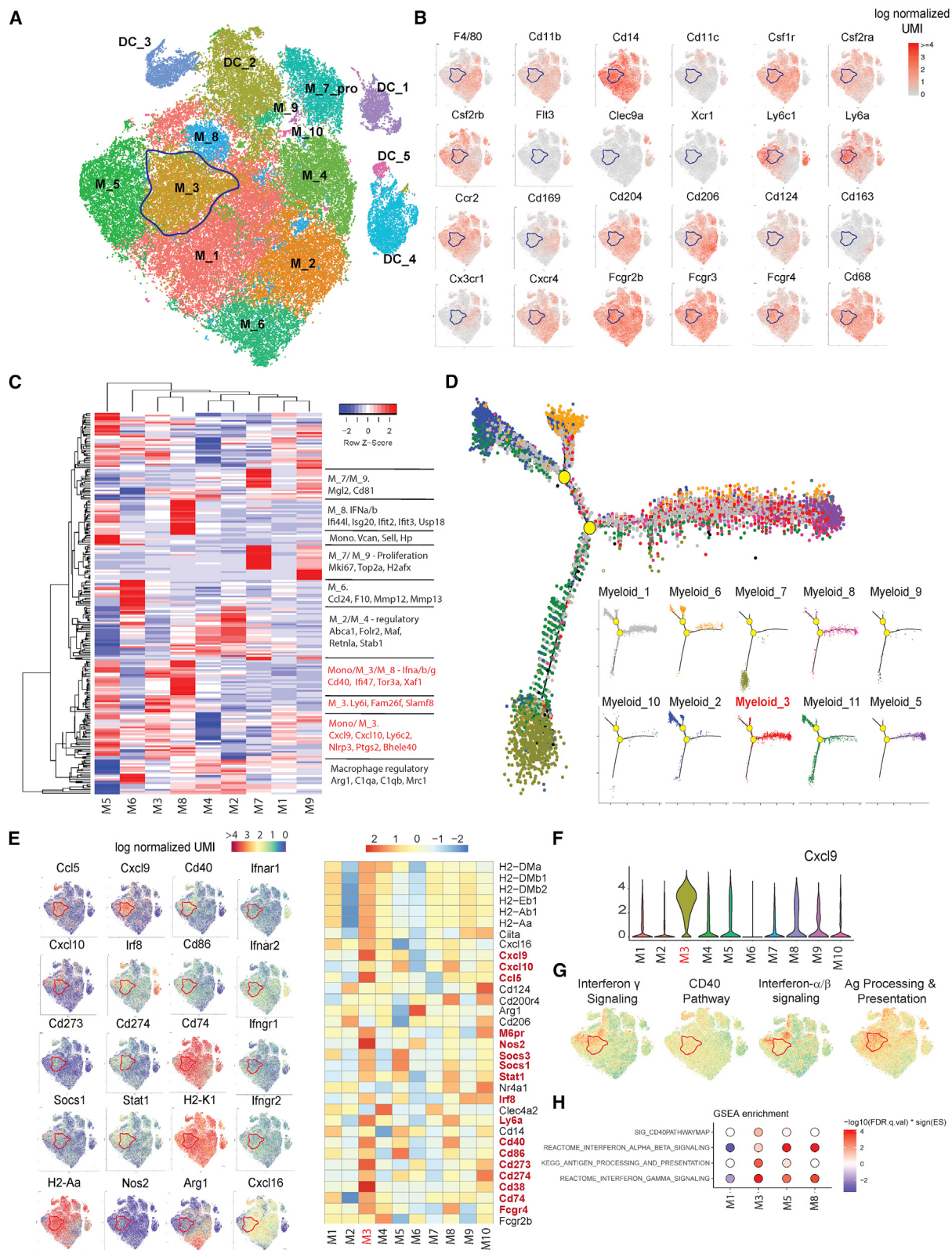


Figure 3. Cxcl9⁺ Monocyte-Derived TAMs Predict Responsiveness to Anti-PD-L1 Therapy (Corrected)

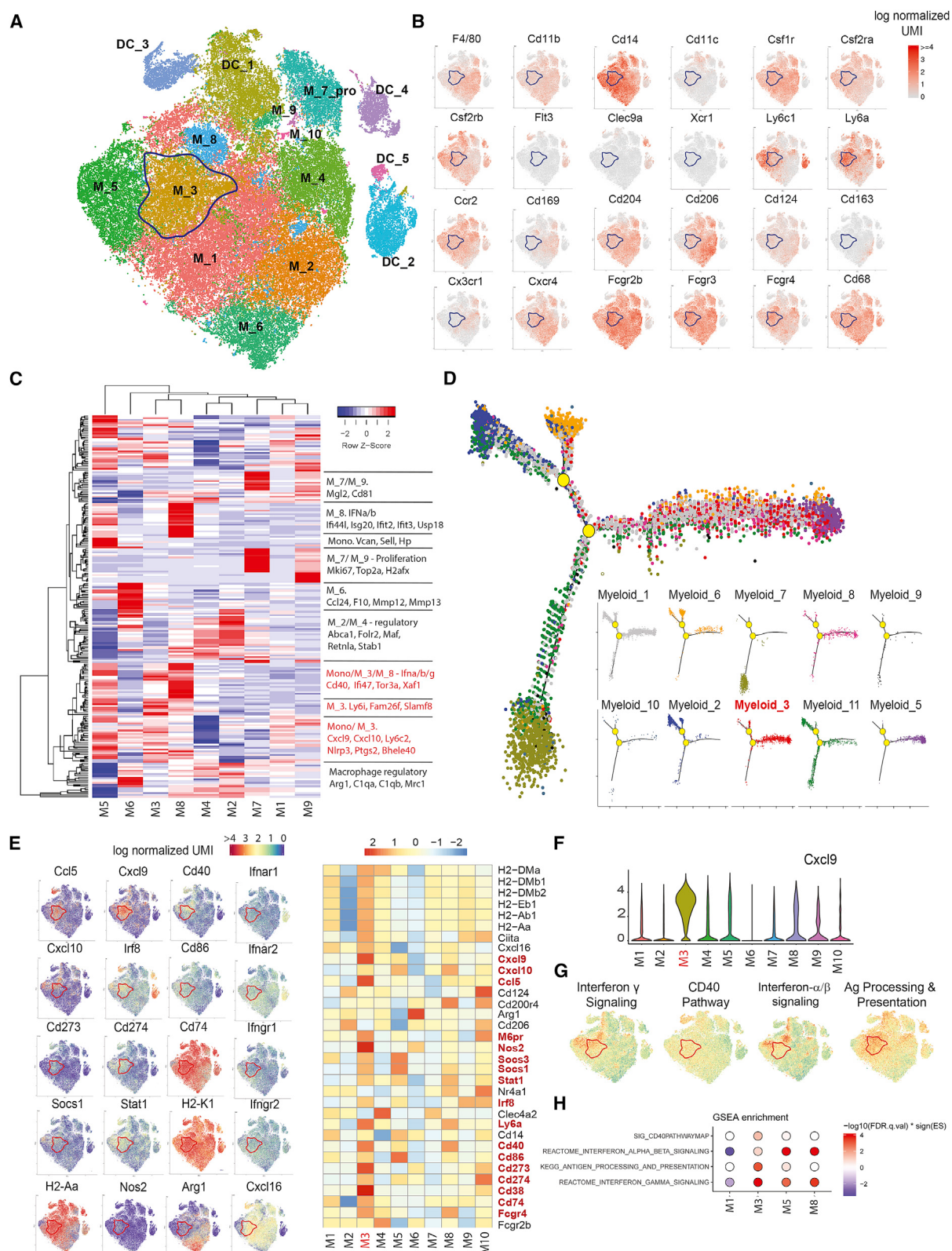


Figure 3. Cxcl9⁺ Monocyte-Derived TAMs Predict Responsiveness to Anti-PD-L1 Therapy (Original)